




Fingerprints of Topotactic Hydrogen in Nickelate Superconductors

Liang Si ^{1,2,*} , Paul Worm ²  and Karsten Held ^{2,*} ¹ School of Physics, Northwest University, Xi'an 710127, China² Institute for Solid State Physics, Vienna University of Technology, 1040 Vienna, Austria; p.worm@a1.net

* Correspondence: liang.si@ifp.tuwien.ac.at (L.S.); held@ifp.tuwien.ac.at (K.H.)

Abstract: Superconductivity has entered the nickel age marked by enormous experimental and theoretical efforts. Notwithstanding, synthesizing nickelate superconductors remains extremely challenging, not least due to incomplete oxygen reduction and topotactic hydrogen. Here, we present density-functional theory calculations for nickelate superconductors with additional topotactic hydrogen or oxygen, namely $\text{La}_{1-x}\text{Sr}_x\text{NiO}_2\text{H}_\delta$ and $\text{LaNiO}_{2+\delta}$. We identify a phonon mode as a possible indication for topotactic hydrogen and discuss the charge redistribution patterns around oxygen and hydrogen impurities.

Keywords: superconductivity; nickelates; strongly correlated electron systems

1. Introduction

Computational materials calculations have predicted superconductivity in nickelates [1] and the heterostructures thereof [2–4] since many decades, mainly based on apparent similarity to cuprate superconductors. Three years ago, superconductivity in nickelates was finally discovered in an experiment by Li, Hwang, and coworkers [5], breaking the grounds for a new age of superconductivity, the nickel age. It is marked by an enormous theoretical and experimental activity, including but not restricted to [5–31]. Superconductivity has been found by now, among others, in $\text{Nd}_{1-x}\text{Sr}_x\text{NiO}_2$ [5,6], $\text{Pr}_{1-x}\text{Sr}_x\text{NiO}_2$ [7], $\text{La}_{1-x}\text{Ca}_x\text{NiO}_2$ [8], $\text{La}_{1-x}\text{Sr}_x\text{NiO}_2$ [9], and most recently in the pentalayer nickelate $\text{Nd}_6\text{Ni}_5\text{O}_{12}$ [10]. Figure 1 shows some of the hallmark experimental critical temperatures (T_c 's) for the nickelates in comparison with the preceding copper [32] and iron age [33] of unconventional superconductivity. Also shown are some other noteworthy superconductors, including the first superconductor, solid Hg, technologically relevant NbTi, and hydride superconductors [34]. The last are superconducting at room temperature [35], albeit only at a pressure of 267 GPa exerted in a diamond anvil cell. All of these compounds are marked in gray in Figure 1 as they are conventional superconductors. That is, the pairing of electrons originates from the electron-phonon coupling, as described in the theory of Bardeen, Cooper, and Schrieffer (BCS) [36].

In contrast, cuprates, nickelates, and, to a lesser extent, iron pnictides are strongly correlated electron systems with a large Coulomb interaction between electrons because of their narrow transition metal orbitals. Their T_c is too high for BCS theory [37,38], and the origin of superconductivity in these strongly correlated systems is still hotly debated. One prospective mechanism is antiferromagnetic spin fluctuations [39–43] stemming from strong electronic correlations. Another mechanism is based on charge density wave fluctuations and received renewed interest with the discovery of charge density wave ordering in cuprates [44,45]. Dynamical vertex approximation [46–49] calculations for nickelates [27], which are unbiased with respect to charge and spin fluctuations, found that spin fluctuations dominated and successfully predicted the superconducting dome prior to experiment in $\text{Nd}_{1-x}\text{Sr}_x\text{NiO}_2$ [6,50,51].



Citation: Si, L.; Worm, P.; Held, K. Fingerprints of Topotactic Hydrogen in Nickelate Superconductors. *Crystals* **2022**, *12*, 656. <https://doi.org/10.3390/cryst12050656>

Academic Editor: Xiaoguan Zhang

Received: 19 April 2022

Accepted: 30 April 2022

Published: 4 May 2022

Publisher's Note: MDPI stays neutral with regard to jurisdictional claims in published maps and institutional affiliations.



Copyright: © 2022 by the authors. Licensee MDPI, Basel, Switzerland. This article is an open access article distributed under the terms and conditions of the Creative Commons Attribution (CC BY) license (<https://creativecommons.org/licenses/by/4.0/>).

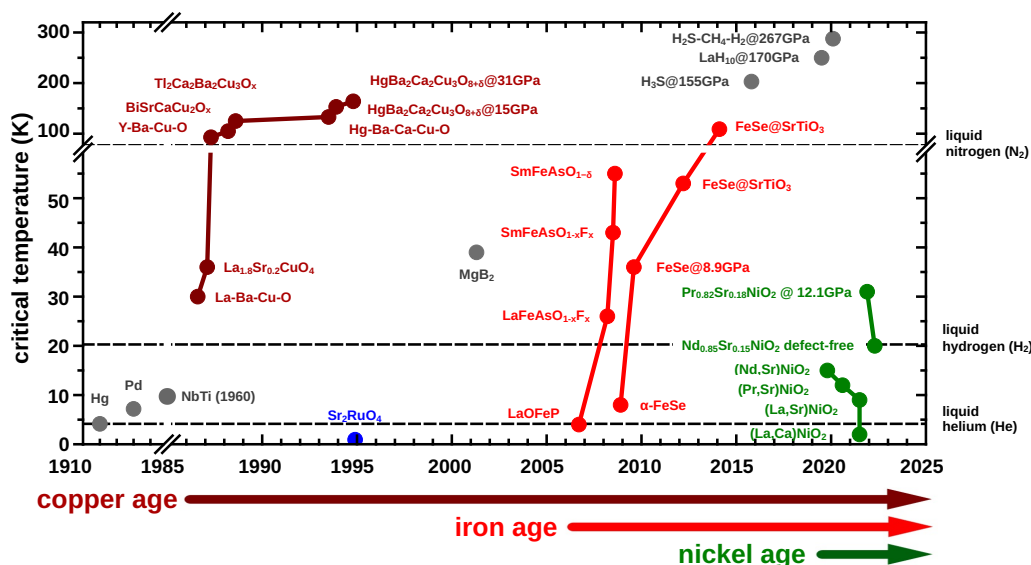


Figure 1. Superconducting T_c vs. year of discovery for selected superconductors. The discovery of cuprates, iron pnictides and nickelates led to enormous experimental and theoretical activities. Hence, one also speaks of the copper, iron and nickel age of superconductivity.

Why did it take 20 years to synthesize superconducting nickelates that have been so seemingly predicted on a computer? To mimic the cuprate Cu $3d^9$ configuration, as in NdNiO_2 , nickel has to be in the uncommon oxidation state Ni^{1+} , which is rare and prone to oxidize further. Only through a complex two-step procedure, Lee, Hwang, and coworkers [52] were able to synthesize superconducting nickelates. In a first step, modern pulsed laser deposition (PLD) was used to grow a $\text{Sr}_x\text{Nd}_{1-x}\text{NiO}_3$ film on a SrTiO_2 substrate. This nickelate is still in the 3D perovskite phase—see Figure 2 (left)—with one oxygen atom too many and will thus not show superconductivity. Hence, this additional oxygen between the layers needs to be removed in a second step. The reducing agent CaH_2 is used to this end within a quite narrow temperature window [52]. If all goes well, one arrives at the superconducting $\text{Sr}_x\text{Nd}_{1-x}\text{NiO}_2$ film (top center). However, this process is prone to incomplete oxidation or to intercalate hydrogen topotactically, i.e., at the position of the removed oxygen; see Figure 2 (bottom center). Both of those unwanted outcomes are detrimental for superconductivity.

In [21,53,54], it was shown by density functional theory (DFT) calculations that NdNiO_2H is indeed energetically favorable to $\text{NdNiO}_2 + 1/2 \text{H}$. For the doped system, on the other hand, $\text{Nd}_{0.8}\text{Sr}_{0.2}\text{NiO}_2$ without the hydrogen intercalated is energetically favorable. The additional H or likewise an incomplete oxidation to $\text{SrNdNiO}_{2.5}$ alters the physics completely. Additional H or $\text{O}_{0.5}$ will remove an electron from the Ni atoms, resulting in Ni^{2+} instead of Ni^{1+} . The formal electronic configuration is hence $3d^8$ instead of $3d^9$, or two holes instead of one hole in the Ni d -shell. Dynamical mean-field theory (DMFT) calculations [21] evidence that the basic atomic configuration is the one of Figure 2 (lower right). That is, because of Hund's exchange, the two holes in NdNiO_2H occupy two different orbitals, $3d_{x^2-y^2}$ and $3d_{3z^2-r^2}$, and form a spin-1. A consequence of this is that DMFT calculations predict NdNiO_2H to be a Mott insulator, whereas NdNiO_2 is a strongly correlated metal with a large mass enhancement of about five [21].

To the best of our knowledge, such a two-orbital, more 3D electronic structure is unfavorable for high- T_c superconductivity. The two-dimensionality of cuprate and nickelate superconductors helps to suppress long-range antiferromagnetic order, while at the same time retaining strong antiferromagnetic fluctuations that can act as a pairing glue for superconductivity. In experiment, we cannot expect ideal NdNiO_2 , NdNiO_2H or $\text{NdNiO}_{2.5}$ films, but most likely some H or additional O will remain in the NdNiO_2 film, after the CaH_2 reduction. Additional oxygen can be directly evidenced in standard X-ray diffraction

analysis after the synthesis step. However, hydrogen, being very light, evades such an X-ray analysis. It has been evidenced in nickelates only by nuclear magnetic resonance (NMR) experiments [55] which, contrary to X-ray techniques, are very sensitive to hydrogen. Ref. [56] suggested hydrogen in LaNiO_2 to be confined at grain boundaries or secondary-phase precipitates. Given these difficulties, it is maybe not astonishing that it took almost one year before a second research group [6] was able to reproduce superconductivity in nickelates. Despite enormous experimental efforts, only a few groups have succeeded hitherto.

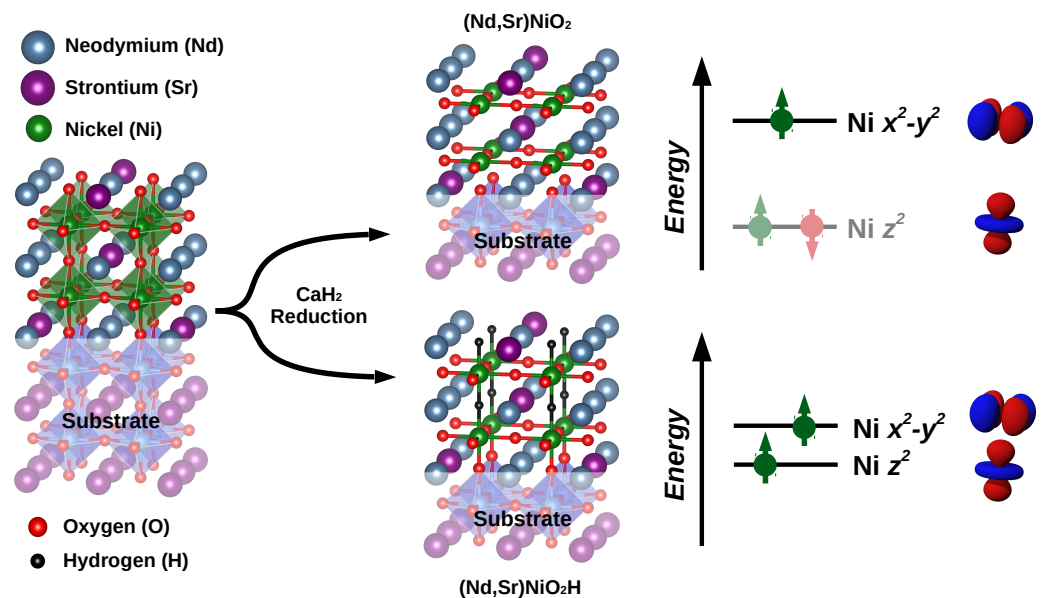


Figure 2. For synthesizing superconducting nickelates (1, left), a perovskite film of $\text{Nd}(\text{La})_{1-x}\text{Sr}_x\text{NiO}_3$ is grown on a SrTiO_3 substrate, and (2, center) the O atoms between the planes are removed by reduction with CaH_2 . Besides the pursued nickelate $\text{Nd}(\text{La})_{1-x}\text{Sr}_x\text{NiO}_2$ (top center), also excess oxygen or topotactic H may remain in the film, yielding $\text{Nd}(\text{La})_{1-x}\text{Sr}_x\text{NiO}_2\text{H}$ (bottom center). The excess hydrogen results in two holes instead of one hole within the topmost two $\text{Ni } 3d$ orbitals (right). Adapted from Ref. [57].

In this paper, we present additional DFT results for topotactic hydrogen and incomplete oxygen reduction in nickelate superconductors: In Section 3, we provide technical information on the DFT calculations. In Section 3, we analyze the energy gain to topotactically intercalate hydrogen in LaNiO_2 and NdNiO_2 . In Section 4, we analyze the phonon spectrum and identify a high-energy mode originating from the Ni-H-Ni bond as a characteristic feature of intercalated hydrogen. In Section 5, we show the changes of the charge distribution caused by topotactic hydrogen or oxygen. Finally, Section 6 provides a summary and outlook.

2. Method

Computational details on E_b . In both our previous theoretical study [21] and this article, the binding energy E_b of hydrogen atoms is computed as:

$$E_b = E[\text{ABO}_2] + \mu[\text{H}] - E[\text{ABO}_2\text{H}]. \quad (1)$$

Here, $E[\text{ABO}_2]$ and $E[\text{ABO}_2\text{H}]$ are the total energy of infinite-layer ABO_2 and hydride-oxides ABO_2H , while $\mu[\text{H}] = E[\text{H}_2]/2$ is the chemical potential of H. Note that H_2 is a typical byproduct for the reduction with CaH_2 and also emerges when CaH_2 is in contact with H_2O . Hence, it can be expected to be present in the reaction. A positive (negative) E_b indicates the topotactic H process is energetically favorable (unfavorable) to obtain ABO_2H instead of ABO_2 and $\text{H}_2/2$.

In the present paper, we go beyond [21] that reported E_b of various ABO_2 compounds by investigating E_b of $La_{1-x}Ca_xNiO_2$ systems for many different doping levels. Here, the increasing Ca-doping is achieved by using the virtual crystal approximation (VCA) [58,59] from $LaNiO_2$ ($x = 0$) to $CaNiO_2$ ($x = 1$). For each Ca concentration, structure relaxation and static total energy calculation is carried out for $La_{1-x}Ca_xNiO_2$ and $La_{1-x}Ca_xNiO_2H$ within the tetragonal space group $P4/mmm$. To this end, we use density-functional theory (DFT) [60,61] with the VASP code [62,63] and the generalized gradient approximations (GGA) of Perdew, Burke, and Ernzerhof (PBE) [64], and PBE revised for solids (PBEsol) [65]. For undoped $LaNiO_2$, the GGA-PBEsol relaxations predict its in-plane lattice constant as 3.890 Å, which is close to that of the STO substrate: 3.905 Å. The computations for $La_{1-x}Ca_xNiO_2$ and $LaCoO_2$, $LaCuO_2$, $SrCoO_2$, and $SrNiO_2$ are performed without spin-polarization and a DFT+ U treatment [66], as the inclusion of Coulomb U and spin-polarization only slightly decrease the E_b by $\sim 5\%$ for $LaNiO_2$ [57]. For $NdNiO_2$, an inevitably computational issue is the localized Nd-4*f* orbitals. These *f*-orbitals are localized around the atomic core, leading to strong correlations. In non-spin-polarized DFT calculations, this generates flat bands near the Fermi level E_F and leads to unsuccessful convergence. To avoid this, we employed DFT+ U [$U_f(Nd) = 7$ eV and $U_d(Ni) = 4.4$ eV] and initialized a G-type anti-ferromagnetic ordering for both Nd- and Ni-sublattice in a $\sqrt{2} \times \sqrt{2} \times 2$ supercell of $NdNiO_2$. For the $Nd_{0.75}Sr_{0.25}NiO_2$ case, 25% Sr-doping is achieved by replacing one out of the four Nd atoms by Sr in a $\sqrt{2} \times \sqrt{2} \times 2$ $NdNiO_2$ supercell.

Computational details on phonons. The phonon computations for $LaNiO_2$, $LaNiO_2H$, $LaNiO_2H_{0.125}$, and $LaNiO_{2.125}$ are performed with the frozen phonon method using the PHONONY [67] code interfaced with VASP. Computations with density functional perturbation theory (DFPT) method [68] are also carried out for double checking. For $LaNiO_2$ and $LaNiO_2H$, the unit cells shown in Figure 3a,b are enlarged to a $2 \times 2 \times 2$ supercell, while for $LaNiO_2H_{0.125}$ and $LaNiO_{2.125}$, the phonons are directly computed with the supercell of Figure 3c,d.

Computational details on electron density. The electron density distributions of $LaNiO_2$, $LaNiO_2H$, $LaNiO_2H_{0.125}$, and $LaNiO_{2.125}$ are computed using the WIEN2K code [69] while taking the VASP-relaxed crystal structure as input. The isosurfaces are plotted from 0.1 (yellow lines) to 2.0 (center of atoms) with spacing of 0.1 in units of $e/\text{Å}^2$.

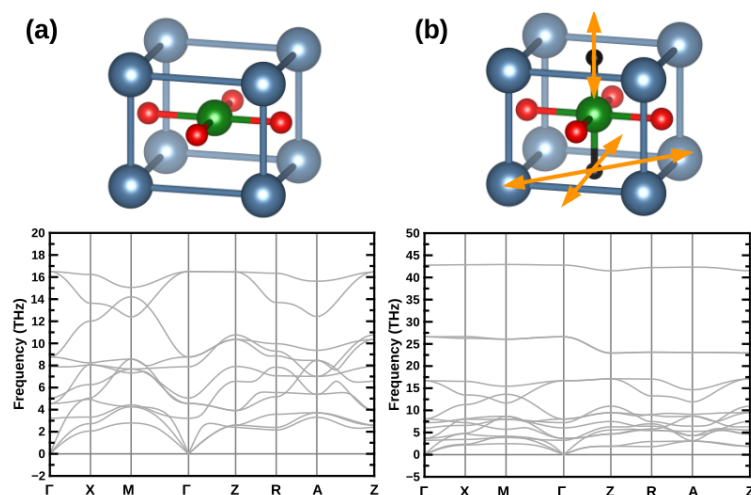


Figure 3. Cont.

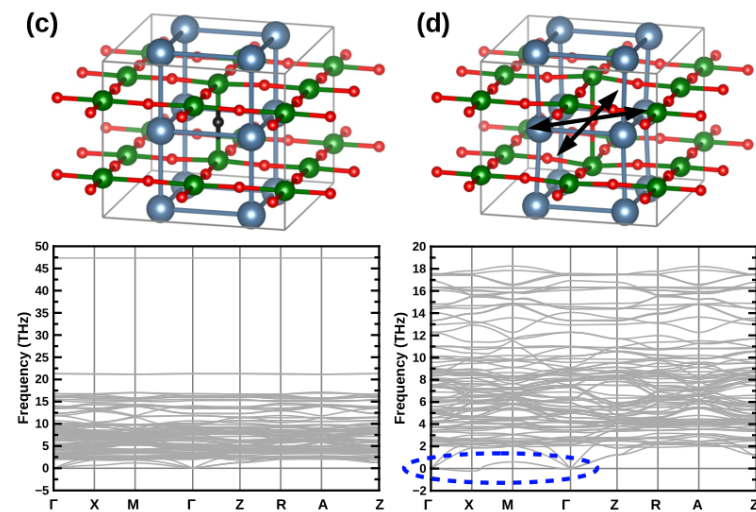


Figure 3. Phonon spectra of (a) LaNiO_2 and (b) LaNiO_2H and in a $2 \times 2 \times 2$ LaNiO_2 supercell doped with a single (c) H and (d) O atom (i.e., $\text{LaNiO}_2\text{H}_{0.125}$ in (c) and $\text{LaNiO}_{2.125}$ in (d)). The orange and black arrows in (b,d) represent vibrations of H and O atoms. The blue dashed oval in (d) labels the unstable phonon modes induced by intercalating additional O atoms in LaNiO_2 .

3. Energetic Stability

Figure 4 shows the results of the hydrogen binding energy E_b for the infinite layer nickelate superconductors $\text{Nd}_{1-x}\text{Sr}_x\text{NiO}_2$ [5,6,50] and $\text{La}_{1-x}\text{Ca}_x\text{NiO}_2$ [8]. To reveal the evolution of E_b when the B-site band filling deviates from their original configurations ($3d^9$ in LaNiO_2 when $x = 0$ and $3d^8$ in CaNiO_2 when $x = 1$), we also show the binding energy of LaCoO_2 ($3d^8$), LaCuO_2 ($3d^{10}$), SrCoO_2 ($3d^7$), and SrNiO_2 ($3d^8$).

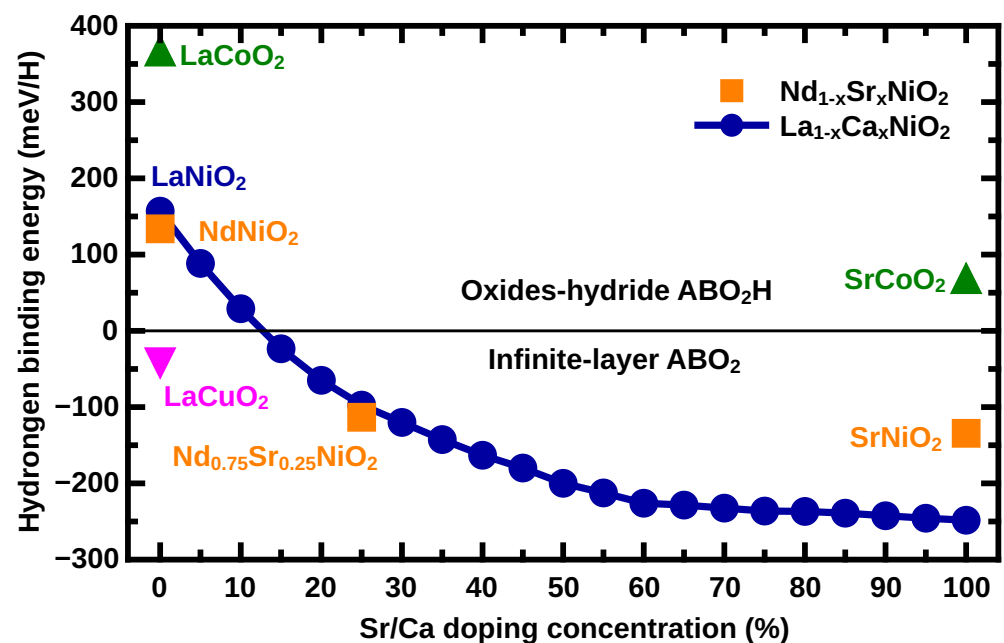


Figure 4. Hydrogen binding energy (E_b) per hydrogen in two nickelate superconductors, $\text{La}_{1-x}\text{Ca}_x\text{NiO}_2$ and $\text{Nd}_{1-x}\text{Sr}_x\text{NiO}_2$ vs. Sr/Ca doping concentration x ; LaCuO_2 , LaCoO_2 , and SrCoO_2 are shown for comparison. Slightly above 10% (Sr,Ca)-doping infinite layer nickelates are energetically more stable. Note that the doping changes the filling of the B-3d orbital. To study the relationship between E_b and the types of B-site elements, E_b of several other ABO_2 compounds is computed: LaCoO_2 , LaCuO_2 , SrCoO_2 and SrNiO_2 . Note that this changes the filling of B-3d orbital within a large range: e.g., $3d^8$ for LaCoO_2 and $3d^9$ for LaNiO_2 .

Let us start with the case of $\text{La}_{1-x}\text{Ca}_x\text{NiO}_2$ [8]. Here, the unoccupied La-4*f* orbitals make the computation possible even without spin-polarization and Coulomb U for La-4*f*, whereas for NdNiO_2 , this is not practicable due to Nd-4*f* flat bands near E_F . Positive (negative) E_b above (below) the horizontal line in Figure 4 indicates topotactic H is energetically favorable (unfavorable). When $x = 0$, i.e., for bulk LaNiO_2 , the system tends to confine H atoms, resulting in oxide-hydride ABO_2H with $E_b = 157$ meV/H. As the concentration of Ca increases, E_b monotonously decreases, reaching -248 meV for the end member of the doping series, CaNiO_2 . The turning point between favorable and unfavorable topotactic H inclusion is around 10% to 15% Ca-doping. Let us note that $E_b = 0$ roughly agrees with the onset of superconductivity, which for Ca-doped LaNiO_2 emerges for $x > 15\%$ Ca-doping [8].

To obtain E_b in NdNiO_2 a much higher computational effort is required: firstly, the Nd-4*f* orbitals must be computed with either treating them as core-states or including spin-splitting. Secondly, for the spin-polarized DFT(+ U) calculations, an appropriate (anti-)ferromagnetic ordering has to be arranged for both Ni- and Nd-sublattices. In oxide-hydride ABO_2H compounds, the δ -type bond between Ni and H stabilizes a G -type anti-ferromagnetic order by driving the system from a quasi two-dimensional (2D) system to a three dimensional (3D) one [21]. Given the large computational costs of E_b for $\text{Nd}_{1-x}\text{Sr}_x\text{NiO}_2$ by using anti-ferromagnetic DFT+ U calculations for both Nd-4*f* ($U \sim 7$ eV) and Ni-3*d* ($U = 4.4$ eV) orbitals, we merely show here the results of NdNiO_2 ($x = 0$), $\text{Nd}_{0.75}\text{Sr}_{0.25}\text{NiO}_2$ ($x = 0.25$), and SrNiO_2 ($x = 1$), which are adopted from [21]. With 25% Sr-doping, the E_b of NdNiO_2 is reduced from 134 meV to -113 meV. Please note that E_b of (Nd,Sr) NiO_2 is slightly smaller than in (La,Ca) NiO_2 , at least in the low doping range. This can be explained by shorter lattice constants in NdNiO_2 , in agreement with the finding [21] that compressive strain plays an important role in reducing E_b .

One can speculate that this suppression of topotactic hydrogen may also play a role when comparing the recently synthesized (Nd,Sr) NiO_2 films on a $(\text{LaAlO}_3)_{0.3}(\text{Sr}_2\text{TaAlO}_6)_{0.7}$ (LSAT) substrate [51] with the previously employed SrTiO_3 (STO) substrate [50]. Lee et al. [51] reported cleaner films without defects and also a higher superconducting transition temperature $T_c \sim 20$ K for the LSAT film as compared to $T_c = 15$ K and plenty of stacking fault defects for the STO substrate [50]. As for (La,Ca) NiO_2 , $E_b = 0$ falls in the region of the onset of the superconductivity for (Sr,Nd) NiO_2 , which is $x \sim 10\%$ Sr-doping in LSAT-strained defect-free films [51] and $x \sim 12.5\%$ at SrTiO_3 -substrate states [50]. Topotactic hydrogen might play a role in suppressing superconductivity in this doping region.

In Figure 4, we further show additional infinite layer compounds LaCoO_2 , LaCuO_2 , SrCoO_2 , and SrNiO_2 for comparison. Their E_b is predicted to be 367, -42 , 69, and -134 meV, respectively. Combining the results of LaNiO_2 and CaNiO_2 , we summarize several tendencies on how to predict E_b of ABO_2 : (1) the strongest effect on E_b is changing the B-site element. However, this seems unpractical for nickelate superconductors as the band filling is strictly restricted to be $3d^{9-x}$ ($x \sim 0.2$). For both trivalent (La, Nd) and bivalent (Sr, Ca) cations, E_b decreases when the B-site cation goes from early to late transition metal elements, e.g., from LaCoO_2 ($3d^8$) to LaNiO_2 ($3d^9$) to LaCuO_2 ($3d^{10}$). (2) Compressive strains induced by either substrate or external pressure can effectively reduce E_b , and we believe that this might be used for growing defect-free films. (3) According to our theoretical calculations, E_b mainly depends on lattice parameters and band filling of the B-site 3*d*-orbitals, but much less on magnetic ordering and Coulomb interaction U .

4. Phonon Dispersion

As revealed by previous DFT phonon spectra calculations [16], NdNiO_2 is dynamically stable. One of the very fundamental questions would be whether topotactic H from over-reacted reduction and/or O from unaccomplished reductive reactions affect the lattice stability. To investigate this point, we perform DFT phonon calculations and analyze the lattice vibration induced by H/O intercalation, as shown in Figure 3.

The phonon spectrum of LaNiO_2 (Figure 3a) is essentially the same as in Ref. [16]; all the phonon frequencies are positive, indicating it is dynamically stable. Its upmost optical phonon at around 14 to 16 THz can be identified with the recent experimental resonant inelastic x-ray scattering (RIXS) data [70] showing a weakly dispersing optical phonon at $\sim 60 \text{ meV} \approx 15 \text{ THz}$. In Figure 3b, the oxides-hydride LaNiO_2H is also predicted to be dynamically stable. Please note that the phonon dispersions between 0 and 20 THz are basically the same as those in LaNiO_2 (Figure 3a; note the different scale of the y -axis). However, one can see new, additional vibration modes from the light H-atoms at frequencies of $\sim 27 \text{ THz}$ and $\sim 43 \text{ THz}$. Among these vibrations, the double degenerate mode at lower frequency is generated by an in-plane (xy -plane) vibration of the topotactic H atom. There are two such in-plane vibrations of H atoms, either along the (100) or (110) direction (and symmetrically related directions), as indicated by the orange arrows in Figure 3b. The mode located at the higher frequency $\sim 43 \text{ THz}$ is, on the other hand, formed by an out-of-plane (z -direction) vibration and is singly degenerate.

We explain these phonon modes in detail by computing the bonding strength between H-1s–Ni- d_{z^2} and H-1s–La- d_{xy} orbitals. Our tight-binding calculations yield an electron hopping term of -1.604 eV between H-1s and Ni- d_{z^2} , while it is -1.052 eV from La- d_{xy} to H-1s. That is, the larger H-1s–Ni- d_{z^2} overlap leads to a stronger δ -type bonding and, together with the shorter c -lattice constant, to a higher phonon energy. Additionally, the shorter c -lattice in LaNiO_2 should also play a role at forming a stronger H-1s–Ni- d_{z^2} bond.

In our previous analysis of the band character for LaNiO_2H [21], the H-1s bands were mainly located at two energy regions: a very flat band that is mostly from the H-1s itself at ~ -7 to -6 eV , and a hybridized band between H-1s and Ni- d_{z^2} at $\sim -2 \text{ eV}$. Together with the higher phonon energy, this indicates that the topotactic H atoms are mainly confined by a Ni sub-lattice via bonding and anti-bonding states formed by H-1s and Ni- d_{z^2} orbitals, instead of the La(Nd) sub-lattice.

The complete (full) topotactic inclusion of H, where all vacancies induced by removing oxygen are filled by H, is an ideal limiting case. Under varying experimental conditions, such as chemical reagent, substrate, temperature, and strain, the H-topotactic inclusion may be incomplete, and thus $\text{ABO}_2\text{H}_\delta$ ($\delta < 1$) may be energetically favored. Hence, we also compute the phonon spectrum at a rather low H-topotactic density: $\text{LaNiO}_2\text{H}_{0.125}$, achieved by including a single H into $2 \times 2 \times 2$ LaNiO_2 supercells as shown in Figure 3c. Moreover, such a local H defect, as revealed by the positive frequency at all q -vectors in the lower panel of Figure 3c, does not destroy the dynamical stability of the LaNiO_2 crystal. In fact, the only remarkable qualitative difference between the complete and 12.5% topotactic H case is the number of phonon bands at 0 THz to 20 THz. This is just a consequence of the larger $2 \times 2 \times 2$ LaNiO_2 supercell, with eight times more phonons. Some quantitative differences can be observed with respect to the energy of the phonon mode: The out-of-plane vibration energy is enhanced from $\sim 43 \text{ THz}$ in LaNiO_2H (Figure 3b) to $\sim 47 \text{ THz}$ in $\text{LaNiO}_2\text{H}_{0.125}$ (Figure 3b), and the in-plane vibration mode frequency is reduced from $\sim 27 \text{ THz}$ in LaNiO_2H (Figure 3b) to $\sim 21 \text{ THz}$ in $\text{LaNiO}_2\text{H}_{0.125}$ (Figure 3c). This is because the H-intercalation shrinks the local c -lattice, i.e., the distance between two Ni atoms separated by topotactic H, from 3.383 \AA in (LaNiO_2H : Figure 3b) to 3.327 \AA ($\text{LaNiO}_2\text{H}_{0.125}$: Figure 3c). The bond length between H and La is, on the other hand, slightly increased from 2.767 \AA in (LaNiO_2H : Figure 3b) to 2.277 \AA ($\text{LaNiO}_2\text{H}_{0.125}$: Figure 3c). This lattice compression (enlargement) explains the enhancement (reduction) for the out-of-plane (in-plane) phonon frequencies (energies).

These results pave a new way to detect the formation of topotactic H in infinite nickelate superconductors: by measuring the phonon modes. The existence of localized phonon modes with little dispersion at $\sim 25 \text{ THz}$ and $\sim 45 \text{ THz}$ indicates the presence of topotactic hydrogen, which otherwise would be extremely hard to detect. These frequencies correspond to energies of 103 meV and 186 meV , respectively, beyond the range $< 80 \text{ meV}$ measured for $\text{La}_{1-x}\text{Sr}_x\text{NiO}_2$ in [71].

Lastly, we further study the case representing an incompleting reduction process: $\text{LaNiO}_{2.125}$, achieved by intercalating a single O into a $2 \times 2 \times 2$ LaNiO_2 supercell ($\text{LaNiO}_{2.125}$: Figure 3d). As the same consequence of employing a supercell in phonon computation, the number of phonon bands is multiplied by a factor of 8 in the frequency region between 0 THz to 20 THz. One obvious difference between undoped LaNiO_2 (Figure 3a) and $\text{LaNiO}_{2.125}$ (Figure 3d) is that the additional O leads to an unstable phonon mode near $q = X(\pi, 0, 0)$ (blue region in Figure 3d). This phonon mode is formed by an effective vibration of the additional O along the xy plane in the (001) or (110) direction (and symmetrically related directions depending on the exact q -vector) of locally cubic coordinate. Such a mode is related to the structural transition from cubic $Pm\bar{3}m$ to a $R\bar{3}c$ rhombohedral phase as in bulk LaNiO_3 , with the Ni-O-Ni bond along the z -direction deviating from 180° . Our simulations for other concentrations of additional O atoms (not shown) also indicate that incomplete oxygen reduction reactions generally result in local instabilities of $\text{LaNiO}_{2+\delta}$ with $\delta > 0$.

5. Charge Distribution

In this section, we perform electron density calculations for LaNiO_2 , LaNiO_2H , $\text{LaNiO}_2\text{H}_{0.125}$, and $\text{LaNiO}_{2.125}$ compounds to investigate the bond types resulting from intercalated H and O atoms. Figure 5a,b show the electron density of LaNiO_2 at the NiO-plane and La-plane (light green planes of the top panels). In Figure 5a, a strong Ni-O bond is observed, while the low electron density between each Ni-O layer reveals a very weak inter-layer coupling, indicating the strong quasi-2D nature of the infinite layer nickelates. In Figure 5b, no bonds are formed between the La (Nd) atoms. The A-site rare-earth elements merely play the role of electron donors.

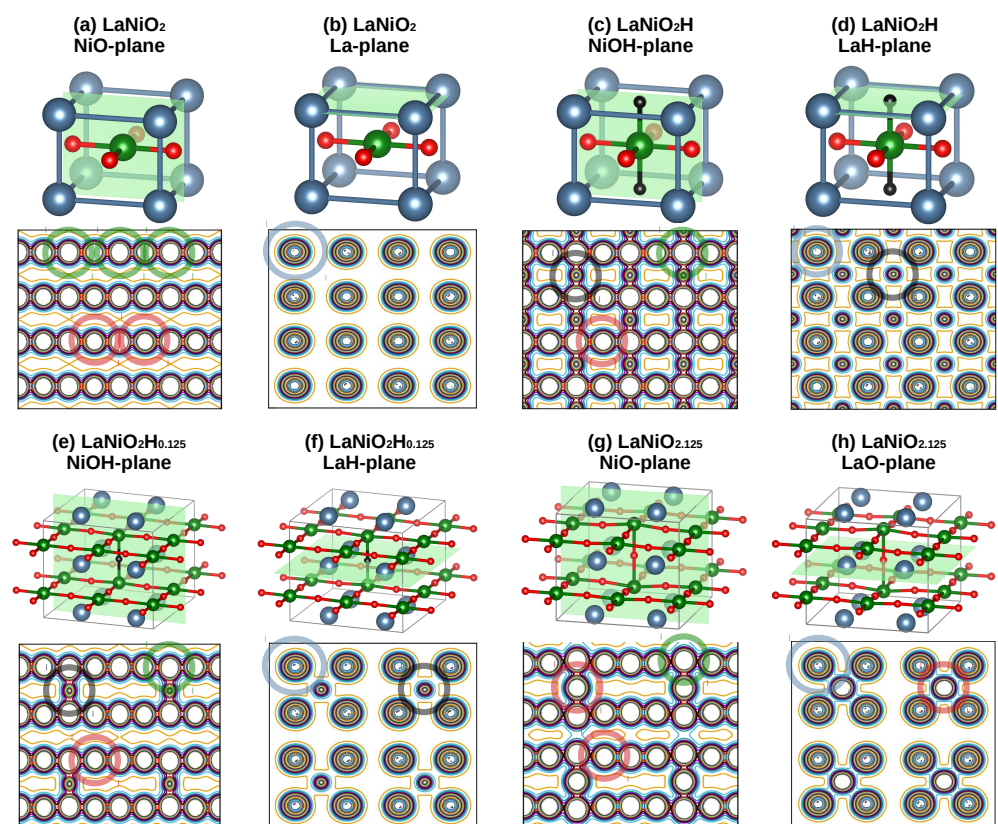


Figure 5. DFT calculated valence charge density of (a,b) LaNiO_2 , (c,d) LaNiO_2H , and a LaNiO_2 supercell doped with a single (e,f) H and (g,h) O atom. For each compound, the charge density of (020) and (001) planes are shown in panels (a,c,e,g) and (b,d,f,h), respectively. The La, Ni, O, and H atoms are labeled by blue, green, red, and black circles, respectively.

Figure 5c,d present the electron density of LaNiO_2H along the same planes. In the NiOH-plane of Figure 5c, the comparison to Figure 5c shows that intercalated H boosts a 3D picture with an additional δ -type bond formed by Ni- d_{z^2} and H-1s orbitals (black circle). Along the LaH-plane (Figure 5d), δ -type bonds are formed by the orbital overlap between La- d_{xy} and H-1s orbitals. For LaNiO_2 with partial topotactic H ($\text{LaNiO}_2\text{H}_{0.125}$ in Figure 5e,f), the additional H atoms play similar roles at the Ni-H and the La-H bonds as in LaNiO_2H . The Ni and La atoms without H in between are similar to those in Figure 5a,b, and those with H are akin to Figure 5c,d. This indicates that the effects induced by topotactic H are indeed very local, i.e., they only affect the nearest Ni and La atoms.

In Figure 5g,h, for $\text{LaNiO}_{2.125}$, the additional O increases the local c -lattice (Ni-Ni bond length via the additional O) from the LaNiO_2 value of 3.338 Å to 4.018 Å which is even larger than the DFT-relaxed value of LaNiO_3 : 3.80 Å. This lattice expansion can be clearly seen in Figure 5g. The large electron density between Ni and O along the z -direction indicates the strength of this Ni-O bond in the z -direction is comparable with the ones along x/y directions. From Figure 5h, we conclude that similar La-O bonds are formed after intercalating additional O atoms, and the La-La distance is shrunken by the additional O atom from 3.889 Å (LaNiO_2) to 3.746 Å between the La atoms pointing to the additional O. However, from the electron density plot, the La-O bond strength seems not stronger than the La-H bonding in Figure 5c,e. This can be explained by the fact that both $O-p_x$ and $-p_y$ orbitals do not point to orbital lobes of La- d_{xy} , leading to a comparable bond strength as the La-H bond in $\text{LaNiO}_2\text{H}_\delta$.

6. Conclusions and Outlook

Our theoretical study demonstrates that the parent compounds of infinite-layer nickelate superconductors, LaNiO_2 and NdNiO_2 , are energetically unstable with respect to topotactic H in the reductive process from perovskite $\text{La}(\text{Nd})\text{NiO}_3$ to $\text{La}(\text{Nd})\text{NiO}_2$. The presence of H, which reshapes the systems from ABO_2 to the hydride-oxide ABO_2H , triggers a transition from a quasi-2D strongly correlated single-band ($d_{x^2-y^2}$) metal, to a two-band ($d_{x^2-y^2}+d_{z^2}$) anti-ferromagnetic 3D Mott insulator. Our predictions [21] have been reproduced by other groups using DFT+ U calculations for other similar ABO_2 systems [53,54]. The recent experimental observation [70] of Ni^{2+} ($3d^8$) in nickelates indicates the existence of topotactic H, as do NMR experiments [55]. The presence of H and its consequence of a 3D Mott-insulator is unfavorable for the emergence of superconductivity in nickelates. However, it is difficult to detect topotactic H in experiment. Three factors contribute to this difficulty: (1) the small radius of H makes it hard to be detected by commonly employed experimental techniques such as X-ray diffraction and scanning transmission electron microscopy (STEM). (2) As revealed by our phonon calculations, the dynamical stability of $\text{La}(\text{Nd})\text{NiO}_2$ does not rely on the concentration of intercalated H atoms. Hence, the same infinite-layer structures should be detected by STEM even in the presence of H. (3) As revealed by electron density distributions, the topotactic H does not break the local crystal structure either (e.g., bond length and angle); the H atoms merely affect the most nearby Ni atoms via a Ni- d_{z^2} -H-1s δ -bond. This is different if we have additional O atoms instead of H: O atoms do not only induce a dynamical instability but also obviously change the local crystal by enlarging the Ni-Ni bond length and angle visibly. Oxygen impurities also lead to unstable phonon modes in $\text{LaNiO}_{2+\delta}$ and thus a major lattice reconstruction.

The ways to avoid topotactic H revealed by our calculations are: in-plane compressive strains and bivalent cation doping with Sr or Ca. This draws our attention to the recently synthesized $(\text{Nd,Sr})\text{NiO}_2$ films [51], which were grown on a $(\text{LaAlO}_3)_{0.3}(\text{Sr}_2\text{TaAlO}_6)_{0.7}$ (LSAT) instead of a SrTiO_3 (STO) substrate, inducing an additional 0.9% compressive strain. These new films were shown to be defect-free and with a considerably larger superconducting dome from 10% to 30% Sr-doping and a higher maximal $T_c \sim 20$ K [51], compared to 12.5%–25% Sr-doping and $T_c \sim 15$ K for nickelate films grown on STO which show many stacking faults [5,6,50]. The compressive strain induced by replacing the STO

substrate ($a = 3.905 \text{ \AA}$) by LSAT ($a = 3.868 \text{ \AA}$) may turn the positive E_b to negative, thus contributing to suppressing defects and recovering a single $d_{x^2-y^2}$ -band picture.

Besides avoiding topotactic H, compressive strain is also predicted as an effective way to enhance T_c . Previous dynamical vertex approximation calculations [27,57] reveal that the key to enhance T_c in nickelates is to enhance the bandwidth W and reduce the ratio of Coulomb interaction U to W . Based on this prediction, we have proposed [27,57] three experimental ways to enhance T_c in nickelates: (1) In-plane compressive strain, which can indeed be achieved by using other substrates having a smaller lattice than STO, such as LSAT (3.868 Å), LaAlO₃ (3.80 Å), or SrLaAlO₄ (3.75 Å). The smaller in-plane lattice shrinks the distance between Ni atoms and thus increases their orbital overlap, leading to a larger W and a smaller U/W . Recent experimental reports have confirmed the validity of this approach by growing (Nd,Sr)NiO₂ on LSAT [51] and Pr_{0.8}Sr_{0.2}NiO₂ on LSAT [72]. (2) Applying external pressure on the films plays the same role as in-plane strain for the, essentially 2D, nickelates. This has been experimentally realized in [73]: under 12.1 GPa pressure, T_c can be enhanced monotonously to 31 K without yet showing a saturation. (3) Replacing $3d$ Ni by $4d$ Pd. In infinite-layer palladates such as NdPdO₂ or LaPdO₂ and similar compounds with 2D PdO₂ layers and separating layers between them, the more extended $4d$ orbitals of Pd are expected to reduce U/W from $U/W \sim 7$ for nickelates to $U/W \sim 6$ for palladates. Further experimental and theoretical research on the electronic and magnetic structure and the superconductive properties of palladates are thus worth performing.

Author Contributions: L.S. and K.H. conceptualized the study; L.S. performed the DFT calculations; L.S., K.H. and P.W. contributed to the writing. All authors have read and agreed to the published version of the manuscript.

Funding: This research has been supported by the Austrian Science Funds (FWF) through project P 32044.

Institutional Review Board Statement: Not applicable.

Informed Consent Statement: Not applicable.

Data Availability Statement: Data will be made available upon reasonable request.

Acknowledgments: We thank M. Kitatani, J. Tomczak, O. Janson and Z. Zhong for valuable discussions and the Austrian Science Funds (FWF) for funding through project P 32044. L.S. also thanks the starting funds from Northwest University. Calculations have been done on the Vienna Scientific Clusters (VSC).

Conflicts of Interest: The authors declare no competing interests.

References

1. Anisimov, V.I.; Bukhvalov, D.; Rice, T.M. Electronic structure of possible nickelate analogs to the cuprates. *Phys. Rev. B* **1999**, *59*, 7901–7906. [[CrossRef](#)]
2. Chaloupka, J.; Khaliullin, G. Orbital Order and Possible Superconductivity in LaNiO₃/LaMO₃ Superlattices. *Phys. Rev. Lett.* **2008**, *100*, 016404. [[CrossRef](#)] [[PubMed](#)]
3. Hansmann, P.; Yang, X.; Toschi, A.; Khaliullin, G.; Andersen, O.K.; Held, K. Turning a Nickelate Fermi Surface into a Cupratelike One through Heterostructuring. *Phys. Rev. Lett.* **2009**, *103*, 016401. [[CrossRef](#)] [[PubMed](#)]
4. Hansmann, P.; Toschi, A.; Yang, X.; Andersen, O.; Held, K. Electronic structure of nickelates: From two-dimensional heterostructures to three-dimensional bulk materials. *Phys. Rev. B* **2010**, *82*, 235123. [[CrossRef](#)]
5. Li, D.; Lee, K.; Wang, B.Y.; Osada, M.; Crossley, S.; Lee, H.R.; Cui, Y.; Hikita, Y.; Hwang, H.Y. Superconductivity in an infinite-layer nickelate. *Nature* **2019**, *572*, 624–627. [[CrossRef](#)]
6. Zeng, S.; Tang, C.S.; Yin, X.; Li, C.; Li, M.; Huang, Z.; Hu, J.; Liu, W.; Omar, G.J.; Jani, H.; et al. Phase Diagram and Superconducting Dome of Infinite-Layer Nd_{1-x}Sr_xNiO₂ Thin Films. *Phys. Rev. Lett.* **2020**, *125*, 147003. [[CrossRef](#)]
7. Osada, M.; Wang, B.Y.; Lee, K.; Li, D.; Hwang, H.Y. Phase diagram of infinite layer praseodymium nickelate Pr_{1-x}Sr_xNiO₂ thin films. *Phys. Rev. Mater.* **2020**, *4*, 121801. [[CrossRef](#)]
8. Zeng, S.; Li, C.; Chow, L.E.; Cao, Y.; Zhang, Z.; Tang, C.S.; Yin, X.; Lim, Z.S.; Hu, J.; Yang, P.; et al. Superconductivity in infinite-layer nickelate La_{1-x}CaxNiO₂ thin films. *Sci. Adv.* **2022**, *8*, eabl9927.

9. Osada, M.; Wang, B.Y.; Goodge, B.H.; Harvey, S.P.; Lee, K.; Li, D.; Kourkoutis, L.F.; Hwang, H.Y. Nickelate Superconductivity without Rare-Earth Magnetism: (La, Sr)NiO₂. *Adv. Mater.* **2021**, *33*, 2104083. [[CrossRef](#)]
10. Pan, G.A.; Segedin, D.F.; LaBollita, H.; Song, Q.; Nica, E.M.; Goodge, B.H.; Pierce, A.T.; Doyle, S.; Novakov, S.; Carrizales, D.C.; et al. Superconductivity in a quintuple-layer square-planar nickelate. *Nat. Mater.* **2022**, *21*, 160–164. [[CrossRef](#)]
11. Botana, A.S.; Norman, M.R. Similarities and Differences between LaNiO₂ and CaCuO₂ and Implications for Superconductivity. *Phys. Rev. X* **2020**, *10*, 011024. [[CrossRef](#)]
12. Sakakibara, H.; Usui, H.; Suzuki, K.; Kotani, T.; Aoki, H.; Kuroki, K. Model Construction and a Possibility of Cupratelike Pairing in a New *d*⁹ Nickelate Superconductor (Nd, Sr)NiO₂. *Phys. Rev. Lett.* **2020**, *125*, 077003. [[CrossRef](#)]
13. Hirayama, M.; Tadano, T.; Nomura, Y.; Arita, R. Materials design of dynamically stable *d*⁹ layered nickelates. *Phys. Rev. B* **2020**, *101*, 075107. [[CrossRef](#)]
14. Hu, L.H.; Wu, C. Two-band model for magnetism and superconductivity in nickelates. *Phys. Rev. Res.* **2019**, *1*, 032046. [[CrossRef](#)]
15. Wu, X.; Di Sante, D.; Schwemmer, T.; Hanke, W.; Hwang, H.Y.; Raghu, S.; Thomale, R. Robust *d*_{x²-y²-wave superconductivity of infinite-layer nickelates. *Phys. Rev. B* **2020**, *101*, 060504. [[CrossRef](#)]}
16. Nomura, Y.; Hirayama, M.; Tadano, T.; Yoshimoto, Y.; Nakamura, K.; Arita, R. Formation of a two-dimensional single-component correlated electron system and band engineering in the nickelate superconductor NdNiO₂. *Phys. Rev. B* **2019**, *100*, 205138. [[CrossRef](#)]
17. Zhang, G.M.; Yang, Y.F.; Zhang, F.C. Self-doped Mott insulator for parent compounds of nickelate superconductors. *Phys. Rev. B* **2020**, *101*, 020501. [[CrossRef](#)]
18. Jiang, M.; Berciu, M.; Sawatzky, G.A. Critical Nature of the Ni Spin State in Doped NdNiO₂. *Phys. Rev. Lett.* **2020**, *124*, 207004. [[CrossRef](#)]
19. Werner, P.; Hoshino, S. Nickelate superconductors: Multiorbital nature and spin freezing. *Phys. Rev. B* **2020**, *101*, 041104. [[CrossRef](#)]
20. Lechermann, F. Late transition metal oxides with infinite-layer structure: Nickelates versus cuprates. *Phys. Rev. B* **2020**, *101*, 081110. [[CrossRef](#)]
21. Si, L.; Xiao, W.; Kaufmann, J.; Tomczak, J.M.; Lu, Y.; Zhong, Z.; Held, K. Topotactic Hydrogen in Nickelate Superconductors and Akin Infinite-Layer Oxides ABO₂. *Phys. Rev. Lett.* **2020**, *124*, 166402. [[CrossRef](#)]
22. Lechermann, F. Multiorbital Processes Rule the Nd_{1-x}Sr_xNiO₂ Normal State. *Phys. Rev. X* **2020**, *10*, 041002. [[CrossRef](#)]
23. Petocchi, F.; Christiansson, V.; Nilsson, F.; Aryasetiawan, F.; Werner, P. Normal State of Nd_{1-x}Sr_xNiO₂ from Self-Consistent GW + EDMFT. *Phys. Rev. X* **2020**, *10*, 041047. [[CrossRef](#)]
24. Adhikary, P.; Bandyopadhyay, S.; Das, T.; Dasgupta, I.; Saha-Dasgupta, T. Orbital-selective superconductivity in a two-band model of infinite-layer nickelates. *Phys. Rev. B* **2020**, *102*, 100501. [[CrossRef](#)]
25. Bandyopadhyay, S.; Adhikary, P.; Das, T.; Dasgupta, I.; Saha-Dasgupta, T. Superconductivity in infinite-layer nickelates: Role of *f* orbitals. *Phys. Rev. B* **2020**, *102*, 220502. [[CrossRef](#)]
26. Karp, J.; Botana, A.S.; Norman, M.R.; Park, H.; Zingl, M.; Millis, A. Many-Body Electronic Structure of NdNiO₂ and CaCuO₂. *Phys. Rev. X* **2020**, *10*, 021061. [[CrossRef](#)]
27. Kitatani, M.; Si, L.; Janson, O.; Arita, R.; Zhong, Z.; Held, K. Nickelate superconductors—A renaissance of the one-band Hubbard model. *NPJ Quantum Mater.* **2020**, *5*, 59. [[CrossRef](#)]
28. Worm, P.; Si, L.; Kitatani, M.; Arita, R.; Tomczak, J.M.; Held, K. Correlations turn electronic structure of finite-layer nickelates upside down. *arXiv* **2021**, arXiv:2111.12697.
29. Geisler, B.; Pentcheva, R. Correlated interface electron gas in infinite-layer nickelate versus cuprate films on SrTiO₃(001). *Phys. Rev. Res.* **2021**, *3*, 013261. [[CrossRef](#)]
30. Klett, M.; Hansmann, P.; Schäfer, T. Magnetic Properties and Pseudogap Formation in Infinite-Layer Nickelates: Insights From the Single-Band Hubbard Model. *Front. Phys.* **2022**, *10*, 834682. [[CrossRef](#)]
31. LaBollita, H.; Botana, A.S. Correlated electronic structure of a quintuple-layer nickelate. *Phys. Rev. B* **2022**, *105*, 085118. [[CrossRef](#)]
32. Bednorz, J.G.; Müller, K.A. Possible high T_C superconductivity in the Ba–La–Cu–O system. *Z. Phys. B Condens. Matter* **1986**, *64*, 189–193. [[CrossRef](#)]
33. Kamihara, Y.; Watanabe, T.; Hirano, M.; Hosono, H. Iron-Based Layered Superconductor La[O_{1-x}F_x]FeAs (*x* = 0.05 – 0.12) with T_c = 26K. *J. Am. Chem. Soc.* **2008**, *130*, 3296. [[CrossRef](#)] [[PubMed](#)]
34. Drozdov, A.P.; Erements, M.I.; Troyan, I.A.; Ksenofontov, V.; Shylin, S.I. Conventional superconductivity at 203 kelvin at high pressures in the sulfur hydride system. *Nature* **2015**, *512*, 73. [[CrossRef](#)]
35. Snider, E.; Dasenbrock-Gammon, N.; McBride, R.; Debessai, M.; Vindana, H.; Vencatasamy, K.; Salamat, K.V.L.A.; Dias, R.P. Room-temperature superconductivity in a carbonaceous sulfur hydride. *Nature* **2020**, *586*, 373. [[CrossRef](#)]
36. Bardeen, J.; Cooper, L.N.; Schrieffer, J.R. Microscopic Theory of Superconductivity. *Phys. Rev.* **1957**, *106*, 162–164. [[CrossRef](#)]
37. Savrasov, S.Y.; Andersen, O.K. Linear-Response Calculation of the Electron-Phonon Coupling in Doped CaCuO₂. *Phys. Rev. Lett.* **1996**, *77*, 4430–4433. [[CrossRef](#)]
38. Boeri, L.; Dolgov, O.V.; Golubov, A.A. Is LaFeAsO_{1-x}F_x an Electron-Phonon Superconductor? *Phys. Rev. Lett.* **2008**, *101*, 026403. [[CrossRef](#)]
39. Scalapino, D.J. A common thread: The pairing interaction for unconventional superconductors. *Rev. Mod. Phys.* **2012**, *84*, 1383–1417. [[CrossRef](#)]

40. Vilardi, D.; Bonetti, P.M.; Metzner, W. Dynamical functional renormalization group computation of order parameters and critical temperatures in the two-dimensional Hubbard model. *Phys. Rev. B* **2020**, *102*, 245128. [[CrossRef](#)]
41. Sordi, G.; Sémon, P.; Haule, K.; Tremblay, A.M.S. Strong Coupling Superconductivity, Pseudogap, and Mott Transition. *Phys. Rev. Lett.* **2012**, *108*, 216401. [[CrossRef](#)]
42. Gull, E.; Millis, A. Numerical models come of age. *Nat. Phys.* **2015**, *11*, 808. [[CrossRef](#)]
43. Kitatani, M.; Schäfer, T.; Aoki, H.; Held, K. Why the critical temperature of high- T_c cuprate superconductors is so low: The importance of the dynamical vertex structure. *Phys. Rev. B* **2019**, *99*, 041115. [[CrossRef](#)]
44. Comin, R.; Damascelli, A. Resonant X-Ray Scattering Studies of Charge Order in Cuprates. *Annu. Rev. Condens. Matter Phys.* **2016**, *7*, 369–405. [[CrossRef](#)]
45. Wu, T.; Mayaffre, H.; Krämer, S.; Horvatić, M.; Berthier, C.; Hardy, W.N.; Liang, R.; Bonn, D.A.; Julien, M.H. Magnetic-field-induced charge-stripe order in the high-temperature superconductor YBa₂Cu₃O_y. *Nature* **2011**, *477*, 191. [[CrossRef](#)]
46. Toschi, A.; Katanin, A.A.; Held, K. Dynamical vertex approximation; A step beyond dynamical mean-field theory. *Phys. Rev. B* **2007**, *75*, 045118. [[CrossRef](#)]
47. Held, K.; Katanin, A.; Toschi, A. Dynamical Vertex Approximation—An Introduction. *Prog. Theor. Phys. (Suppl.)* **2008**, *176*, 117. [[CrossRef](#)]
48. Katanin, A.A.; Toschi, A.; Held, K. Comparing pertinent effects of antiferromagnetic fluctuations in the two- and three-dimensional Hubbard model. *Phys. Rev. B* **2009**, *80*, 075104. [[CrossRef](#)]
49. Rohringer, G.; Hafermann, H.; Toschi, A.; Katanin, A.A.; Antipov, A.E.; Katsnelson, M.I.; Lichtenstein, A.I.; Rubtsov, A.N.; Held, K. Diagrammatic routes to nonlocal correlations beyond dynamical mean field theory. *Rev. Mod. Phys.* **2018**, *90*, 025003. [[CrossRef](#)]
50. Li, D.; Wang, B.Y.; Lee, K.; Harvey, S.P.; Osada, M.; Goodge, B.H.; Kourkoutis, L.F.; Hwang, H.Y. Superconducting Dome in Nd_{1-x}Sr_xNiO₂ Infinite Layer Films. *Phys. Rev. Lett.* **2020**, *125*, 027001. [[CrossRef](#)]
51. Lee, K.; Wang, B.Y.; Osada, M.; Goodge, B.H.; Wang, T.C.; Lee, Y.; Harvey, S.; Kim, W.J.; Yu, Y.; Murthy, C.; et al. Character of the “normal state” of the nickelate superconductors. *arXiv* **2022**, arXiv:2203.02580.
52. Lee, K.; Goodge, B.H.; Li, D.; Osada, M.; Wang, B.Y.; Cui, Y.; Kourkoutis, L.F.; Hwang, H.Y. Aspects of the synthesis of thin film superconducting infinite-layer nickelates. *APL Mater.* **2020**, *8*, 041107. [[CrossRef](#)]
53. Malyi, O.I.; Varignon, J.; Zunger, A. Bulk NdNiO₂ is thermodynamically unstable with respect to decomposition while hydrogenation reduces the instability and transforms it from metal to insulator. *Phys. Rev. B* **2022**, *105*, 014106. [[CrossRef](#)]
54. Bernardini, F.; Bosin, A.; Cano, A. Geometric effects in the infinite-layer nickelates. *arXiv* **2021**, arXiv:2110.13580.
55. Cui, Y.; Li, C.; Li, Q.; Zhu, X.; Hu, Z.; feng Yang, Y.; Zhang, J.; Yu, R.; Wen, H.H.; Yu, W. NMR Evidence of Antiferromagnetic Spin Fluctuations in Nd_{0.85}Sr_{0.15}NiO₂. *Chin. Phys. Lett.* **2021**, *38*, 067401. [[CrossRef](#)]
56. Puphal, P.; Pomjakushin, V.; Ortiz, R.A.; Hammoud, S.; Isobe, M.; Keimer, B.; Hepting, M. Investigation of Hydrogen Incorporations in Bulk Infinite-Layer Nickelates. *Front. Phys.* **2022**, *10*, 842578. [[CrossRef](#)]
57. Held, K.; Si, L.; Worm, P.; Janson, O.; Arita, R.; Zhong, Z.; Tomczak, J.M.; Kitatani, M. Phase Diagram of Nickelate Superconductors Calculated by Dynamical Vertex Approximation. *Front. Phys.* **2022**, *9*, 810394. [[CrossRef](#)]
58. Bellaiche, L.; Vanderbilt, D. Virtual crystal approximation revisited: Application to dielectric and piezoelectric properties of perovskites. *Phys. Rev. B* **2000**, *61*, 7877–7882. [[CrossRef](#)]
59. Eckhardt, C.; Hummer, K.; Kresse, G. Indirect-to-direct gap transition in strained and unstrained Sn_xGe_{1-x} alloys. *Phys. Rev. B* **2014**, *89*, 165201. [[CrossRef](#)]
60. Hohenberg, P.; Kohn, W. Inhomogeneous Electron Gas. *Phys. Rev.* **1964**, *136*, B864–B871. doi: 10.1103/PhysRev.136.B864. [[CrossRef](#)]
61. Kohn, W.; Sham, L.J. Self-Consistent Equations Including Exchange and Correlation Effects. *Phys. Rev.* **1965**, *140*, A1133–A1138. [[CrossRef](#)]
62. Kresse, G.; Hafner, J. Ab initio molecular dynamics for liquid metals. *Phys. Rev. B* **1993**, *47*, 558–561. [[CrossRef](#)]
63. Kresse, G.; Furthmüller, J. Efficiency of ab-initio total energy calculations for metals and semiconductors using a plane-wave basis set. *Comput. Mater. Sci.* **1996**, *6*, 15–50. [[CrossRef](#)]
64. Perdew, J.P.; Burke, K.; Ernzerhof, M. Generalized Gradient Approximation Made Simple. *Phys. Rev. Lett.* **1996**, *77*, 3865–3868. [[CrossRef](#)]
65. Perdew, J.P.; Ruzsinszky, A.; Csonka, G.I.; Vydrov, O.A.; Scuseria, G.E.; Constantin, L.A.; Zhou, X.; Burke, K. Restoring the Density-Gradient Expansion for Exchange in Solids and Surfaces. *Phys. Rev. Lett.* **2008**, *100*, 136406. [[CrossRef](#)]
66. Anisimov, V.I.; Zaanen, J.; Andersen, O.K. Band theory and Mott insulators: Hubbard U instead of Stoner I. *Phys. Rev. B* **1991**, *44*, 943–954. [[CrossRef](#)]
67. Togo, A.; Tanaka, I. First principles phonon calculations in materials science. *Scr. Mater.* **2015**, *108*, 1–5. [[CrossRef](#)]
68. Baroni, S.; de Gironcoli, S.; Dal Corso, A.; Giannozzi, P. Phonons and related crystal properties from density-functional perturbation theory. *Rev. Mod. Phys.* **2001**, *73*, 515–562. [[CrossRef](#)]
69. Blaha, P.; Schwarz, K.; Madsen, G.; Kvasnicka, D.; Luitz, J. wien2k. In *An Augmented Plane Wave+ Local Orbitals Program for Calculating Crystal Properties*; Vienna University of Technology: Vienna, Austria, 2001.
70. Krieger, G.; Martinelli, L.; Zeng, S.; Chow, L.; Kummer, K.; Arpaia, R.; Sala, M.M.; Brookes, N.; Ariando, A.; Viart, N.; et al. Charge and spin order dichotomy in NdNiO₂ driven by SrTiO₃ capping layer. *arXiv* **2021**, arXiv:2112.03341.
71. Rossi, M.; Osada, M.; Choi, J.; Agrestini, S.; Jost, D.; Lee, Y.; Lu, H.; Wang, B.Y.; Lee, K.; Nag, A.; et al. A Broken Translational Symmetry State in an Infinite-Layer Nickelate. *arXiv* **2021**, arXiv:2112.02484.

-
72. Ren, X.; Gao, Q.; Zhao, Y.; Luo, H.; Zhou, X.; Zhu, Z. Superconductivity in infinite-layer $\text{Pr}_{0.8}\text{Sr}_{0.2}\text{NiO}_2$ films on different substrates. *arXiv* **2021**, arXiv:2109.05761.
 73. Wang, N.; Yang, M.; Chen, K.; Yang, Z.; Zhang, H.; Zhu, Z.; Uwatoko, Y.; Dong, X.; Jin, K.; Sun, J.; et al. Pressure-induced monotonic enhancement of T_c to over 30 K in the superconducting $\text{Pr}_{0.82}\text{Sr}_{0.18}\text{NiO}_2$ thin films. *arXiv* **2021**, arXiv:2109.12811.